nature photonics

Article

https://doi.org/10.1038/s41566-022-01151-3

Gigantic suppression of recombination rate in 3D lead-halide perovskites for enhanced photodetector performance

Received: 10 July 2020

Accepted: 19 December 2022

Published online: 16 February 2023

Check for updates

Kwang Jin Lee[1,3] ✉, Ran Wei[1], Ye Wang[2], Jihua Zhang[1,4], Wenchi Kong[2], Sandeep Kumar Chamoli[2], Tao Huang[2], Weili Yu[2], Mohamed ElKabbash[1,5] ✉ & Chunlei Guo[1] ✉

Prolonging the carrier lifetime in lead-halide perovskite (LHP) can enable novel schemes for highly efficient energy-harvesting and photodetection applications. However, suppressing the recombination processes in LHP without chemical treatments remains an open challenge. Here we show that the recombination rate of three-dimensional LHP polycrystalline thin films can decrease significantly when placed on hyperbolic metamaterials. Through momentum-resolved imaging, we reveal that these LHP films possess a dominant in-plane transition dipole, which in turn is responsible for the decrease in the recombination rate. We observe a decrease in the recombination rate of a $MAPbI_3$ LHP thin film by ~50% and 30% when placed on a plasmonic mirror and a hyperbolic metamaterial, respectively. Furthermore, we discover a tenfold decrease in the recombination rate of $(Cs_{0.06}FA_{0.79}MA_{0.15})Pb(I_{0.85}Br_{0.15})_3$, and the origin of this giant reduction in the recombination process is discussed based on exciton-trapping dynamics. By controlling the recombination rate of LHPs, we demonstrate a 250% increase in photoresponsivity of LHP-based photodetectors. The resulting physical insights will provide novel means to enhance the efficiency of LHP-based optoelectronic and photonic devices.

Photoluminescence (PL) plays a crucial role in determining the performance of light- and energy-harvesting devices. Fundamentally, PL from excited emitters takes place due to vacuum fluctuations where the emitters interact with their local electromagnetic fields[1–5]. According to Fermi's golden rule, the recombination rate is proportional to the number of available propagating or evanescent electromagnetic modes to which the emitters can decay, that is, the local density of optical states (LDOS)[1]. Purcell introduced the idea of controlling the emission rate of an emitter by placing it inside a cavity that can alter the LDOS[6]. The Purcell factor (PF) quantifies the ratio of the modified radiative decay rate to that in free space.

Controlling the PF is of fundamental importance to photonic devices where the device efficiency is sensitive to the recombination dynamics[1,7–9]. Various nanophotonic platforms have been utilized to enhance the PF, for example, photonic-crystal cavities[8], low-modal-volume plasmonic nanocavities[10] and high-LDOS structures such as hyperbolic metamaterials[3–5]. On the other hand, reduction of the PF has been realized by means of photonic-bandgap materials[11,12]

[1]The Institute of Optics, University of Rochester, Rochester, NY, USA. [2]GPL, Changchun Institute of Optics, Fine Mechanics and Physics, Chinese Academy of Sciences, Changchun, China. [3]Present address: Center for Molecular Spectroscopy and Dynamics, Institute for Basic Science (IBS), Seoul, Republic of Korea. [4]Present address: ARC Centre of Excellence for Transformative Meta-Optical Systems (TMOS), Research School of Physics, The Australian National University, Canberra, Australia. [5]Present address: Research Laboratory of Electronics, MIT, Cambridge, MA, USA. ✉e-mail: kwangjin.lee1028@gmail.com; melkabba@mit.edu; guo@optics.rochester.edu

or cavities with an optical length smaller than half the emitter wavelength[13]. In addition to the design of platforms with engineered LDOS, the transition dipole orientation of the emitter can play a critical role in determining the recombination rate[14]. A common assumption, however, is that the transition dipole moment of an emitter is isotropic, that is, with no preferred orientation. This assumption is not always valid and may lead to discrepancies between the predicted recombination rate and the measured one[15–17]. Recent works have reported that several two-dimensional (2D) luminescent materials show strong anisotropic (in-plane or out-of-plane) dipole orientation[15,16,18–21]. Directional emission due to optical anisotropy is important to enhance the performance of optoelectronic devices, lasing and displays[21,22].

Lead-halide perovskites (LHPs) are an exciting class of semiconductors with remarkable optical and electronic properties, such as strong light absorption, low surface recombination rates[23] and long charge-carrier diffusion lengths[24,25]. These properties have led to LHPs becoming the focus of fundamental and applied research to develop high-efficiency optoelectronic devices such as photodetectors[26–29], photovoltaics[30–32] and light-emitting devices[33–35]. Understanding the nature of excitons in LHPs is thus of major importance for the realization of high-efficiency LHP-based devices.

In this Article, we first characterize the transition dipole orientation of an LHP film ($MAPbI_3$, MA = CH_3NH_3) through a momentum-resolved imaging technique. The anisotropic (in-plane) nature of the transition dipole in the LHP film allows us to control its recombination rate using plasmonic materials via two competing effects: increasing the recombination rate (Purcell enhancement) due to the excitation of evanescent (high-k, k is the wavevector, indicating momentum of light) modes, and decreasing the recombination rate (Purcell inhibition) due to the suppression of propagating modes as a result of a destructive interaction between the transition dipole and its out-of-phase image. We observe a significant decrease in the recombination rate in the $MAPbI_3$ film, even when it is deposited directly on a hyperbolic metamaterial (HMM), which is contrary to all existing literature on quantum metamaterials[3–5,36–38]. We note that the destructive interaction between the in-plane transition dipole and its image reduce the LDOS by decreasing the amplitude of the net transition dipole moment. We further demonstrate that this scalable and purely physical approach can substantially prolong the PL lifetime, which leads to an increase in the carrier diffusion length in the $MAPbI_3$ film by up to 43%. Most strikingly, we obtain a tenfold reduction of the PF (900% increase in the PL lifetime) in a triple-cation LHP (TCLHP, $(Cs_{0.06}FA_{0.79}MA_{0.15})\,Pb(I_{0.85}Br_{0.15})_3$) film when it is deposited on a plasmonic mirror. We utilize the enhanced carrier diffusion length to improve the performance of LHP-based photodetectors and realize a 250% enhancement in photoresponsivity.

Results

Image dipole interaction effect on recombination rate

Figure 1a schematically shows the material configuration and the mechanisms that determine the PF of an emitter interacting with a plasmonic substrate. In general, the recombination rate of a transition dipole at a distance d away from a metallic surface experiences two effects. For small d ($\ll\lambda$, wavelength), the dipole's near-field is capable of exciting high-k (evanescent) modes such as the surface plasmon polaritons (SPPs) that propagate at the metal–dielectric interface and the bulk plasmon polaritons (BPPs) that propagate inside HMMs. Excitation of such high-k and non-radiative modes will increase the recombination rate, regardless of the dipole orientation. As d increases, the interaction between the dipole and its image formed by the metal layer comes into play and can alter the recombination rate depending on the transition dipole orientation. For a proper range of d, the destructive interaction between the radiation from an in-plane dipole and its (out-of-phase) image dipole decreases the LDOS by suppressing the excitation of radiation (propagating) modes. Conversely, the constructive interaction between the radiation from an out-of-plane dipole and its (in-phase) image dipole increases the LDOS by enhancing the excitation of radiation modes. The effect of the image dipole interaction diminishes as d increases[14].

To describe this interaction, we calculated the PFs for in-plane and isotropic dipoles placed at a distance d from a silver mirror at visible wavelengths, as shown in Fig. 1b and 1c, respectively. For an in-plane dipole at $d < 20$ nm, the recombination rate is accelerated (PF > 1) as the emitter excites SPPs. Interestingly, for $\lambda \gtrsim 650$ nm and a certain range of d, PF < 1 is possible for the in-plane dipole case. On the other hand, the PF is always larger than 1 for an isotropic dipole. The higher PF of the isotropic dipole for $d < 20$ nm compared to an in-plane dipole occurs because the out-of-plane component further boosts the PF at short distances; that is, the constructive interaction between the out-of-plane component and its image increases the PF in addition to the excitation of surface waves on the metallic substrates (Supplementary Note I and Supplementary Fig. 1)[14]. Note that the relative phase between the radiation from the dipole and its image is given by $2\pi d/n\lambda$, where n is the refractive index of the environment. Consequently, at a given distance d, the effect of the image dipole interaction on the LDOS accentuates as λ increases. Figure 1d and 1e presents the PF calculation for in-plane and isotropic dipole orientations as a function of d and λ in the presence of an HMM, respectively. Surprisingly, there exists a spectral and spatial range where PF < 1, even on an HMM in the case of an in-plane dipole, contrary to reports from the existing literature on HMMs. Note that the spectral and spatial range where PF > 1 is wider than the mirror case owing to the high-k BPP modes supported by HMMs, which further increases the LDOS[36]. In Supplementary Note II, we discuss the generalized image dipole concept and the difference between the image dipole interaction with a metallic mirror and the interference effect with dielectric mirrors to realize a lower PF (Supplementary Figs. 2 and 3).

We deposited LHPs on various substrates to study the exciton properties of the LHP films. We note that LHPs sustain excitonic transitions and a large oscillator strength, which are prerequisite conditions for the examination of dipole orientation[39–41] (Supplementary Note III). The linear absorption spectrum of the $MAPbI_3$ film enables a strong excitonic contribution to a radiative band-to-band transition, despite its small exciton binding energy of 33 meV (Supplementary Fig. 4a and Supplementary Table 1). The solution-processed fabrication of LHPs provides a straightforward approach for integration with nanophotonic structures such as plasmonic mirrors and HMMs, which have been used to engineer the recombination rate of various quantum emitters[42–44]. In our experiments, we spin-coated 60-nm-thick emitter films on glass, a single-pair $Ag–Al_2O_3$ film (plasmonic mirror) and a four-pair $Ag–Al_2O_3$ HMM. The thicknesses of the Ag and Al_2O_3 films are both 10 nm (Supplementary Fig. 5). The PL spectra and Raman spectra of $MAPbI_3$ films deposited on both glass and HMM show no notable dependence of the LHP film properties on the substrate (Supplementary Fig. 6).

Far-field radiation pattern measurements

To study the effect of transition dipole orientation on the PL decay dynamics, we performed a comparative study of $MAPbI_3$ and organic dye (LDS750) thin films. We chose LDS750 because its PL spectrum overlaps with that of $MAPbI_3$ (Fig. 2a). To determine the transition dipole orientation of both emitters, we carried out measurements of the far-field radiation pattern for $MAPbI_3$ and LDS750 films using a momentum-resolved imaging technique[15,18] (details of the experimental set-up and simulation method are provided in Supplementary Fig. 7 and Supplementary Note IV). Figure 2b and 2c presents the measured and calculated far-field radiation patterns of the LDS750 and $MAPbI_3$ films, respectively. In general, the p-polarized momentum-resolved PL ($I^p(k_\parallel)$) collected from an ensemble of dipoles can be modelled as a superposition of in-plane ($I^p_{IP}(k_\parallel)$) and out-of-plane ($I^p_{OP}(k_\parallel)$) dipole emission such that[18]

$$I^p(k_\parallel) = A\left[\alpha I^p_{IP}(k_\parallel) + (1-\alpha)\, I^p_{OP}(k_\parallel)\right] \quad (1)$$

https://doi.org/10.1038/s41566-022-01151-3

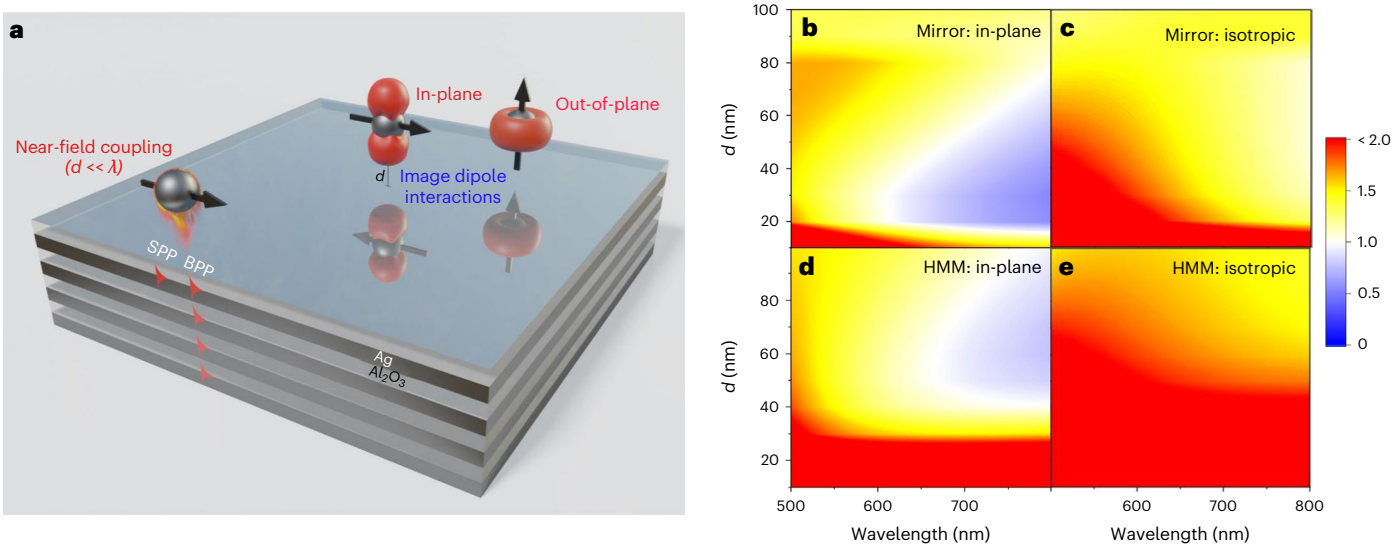

Fig. 1 | Purcell effect of an anisotropic transition dipole in the presence of a plasmonic substrate. a, Schematic description of the material configuration and underlying mechanisms of the optical interplay between the transition dipole and plasmonic substrates. When $d \ll \lambda$, the dipole's near-field excites SPPs in metallic substrates and BPPs in HMMs, increasing the PF regardless of the dipole orientation. As d increases slightly, the interaction between the transition dipole and its image formed on the substrate strongly influences the LDOS by decreasing the net transition dipole moment depending on the dipole's orientation and position. For reasonably close dipoles, a destructive interaction occurs between an in-plane dipole and its out-of-phase image dipole, which reduces the LDOS pertaining to propagating modes. Conversely, a constructive interaction occurs between an out-of-plane dipole and its in-phase image dipole, which increases its LDOS by increasing the net transition dipole moment. **b**,**c**, Numerical calculation of PF (colour bar) as a function of d and wavelength in the presence of a mirror for in-plane and isotropic dipole orientations. **d**,**e**, Numerical calculation of PF (colour bar) as a function of d and wavelength in the presence of an HMM for in-plane (**d**) and isotropic (**e**) dipole orientations. Note the existence of a region in the parameter space of an in-plane dipole on a mirror (**b**) and an HMM (**d**), where PF < 1. Isotropic dipole orientation is defined as $(2\gamma_{IP} + \gamma_{OP})/3$ where γ_{IP} and γ_{OP} are in-plane and out-of-plane dipoles, respectively[14].

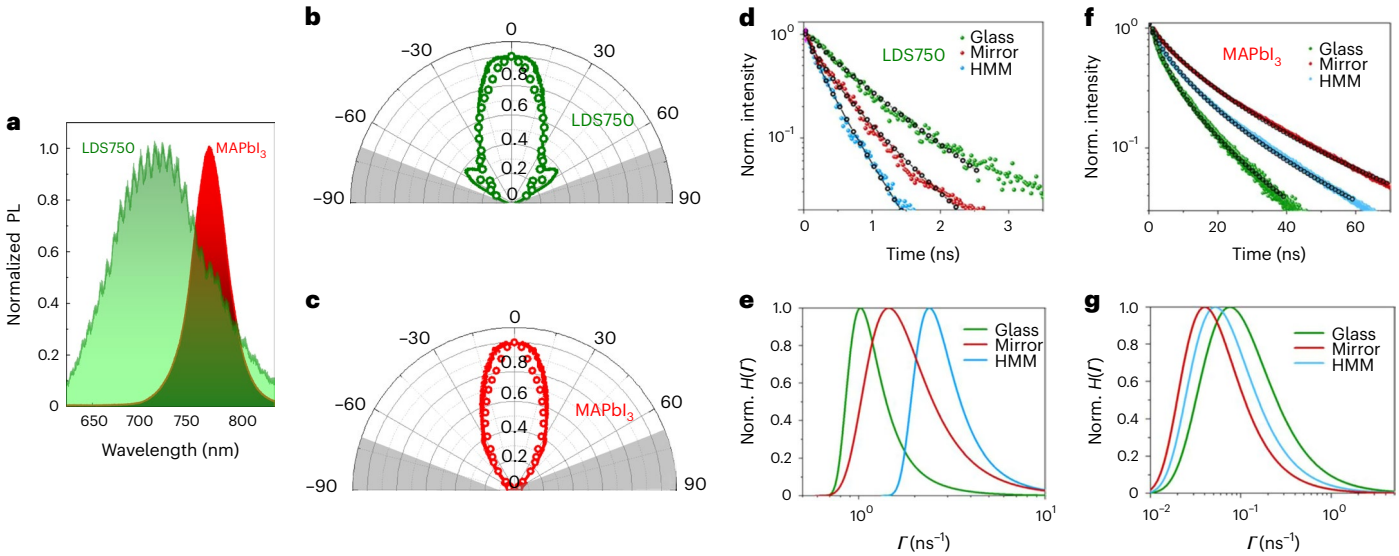

Fig. 2 | Momentum-resolved radiation and TRPL measurements of $MAPbI_3$ and LDS750 films. a, PL spectra of $MAPbI_3$ (red) and LDS750 (green) films deposited on glass at 532-nm excitation. **b**,**c**, Radiation patterns of the same LDS750 (**b**) and $MAPbI_3$ (**c**) films as a function of the emission angle, respectively. Solid curves and open circles correspond to experimental and simulation results, respectively. Grey regions represent the angular range that was not collected. **d**,**e**, Experimental results of normalized TRPL (**d**) and normalized recombination rate distribution ($H(\Gamma)$) (**e**) of $MAPbI_3$ polycrystalline film deposited on glass, mirror and HMM substrates. **f**,**g**, Experimental result of normalized TRPL (**f**) and normalized $H(\Gamma)$ (**g**) of LDS750 film deposited on glass, mirror and HMM substrates. The excitation wavelength for TRPL is 532 nm. The filled black circles in **d** and **f** are fitting curves based on the stretched exponential function.

where A is a proportionality constant that depends on experimental parameters such as the integration time and excitation intensity, and $k_{\parallel}$ is the in-plane photon momentum. α represents the ratio of $I_{IP}^{p}(k_{\parallel})$ to the total emission. By fitting the momentum-resolved PL with equation (1), we estimated α for $MAPbI_3$ and LDS750 to be ~1 ± 0.0027 and ~0.86 ± 0.0037, respectively. This explicitly indicates that the PL collected from $MAPbI_3$ originates mainly from in-plane excitons, whereas LDS750 represents a near-isotropic emitter. The exciton

https://doi.org/10.1038/s41566-022-01151-3

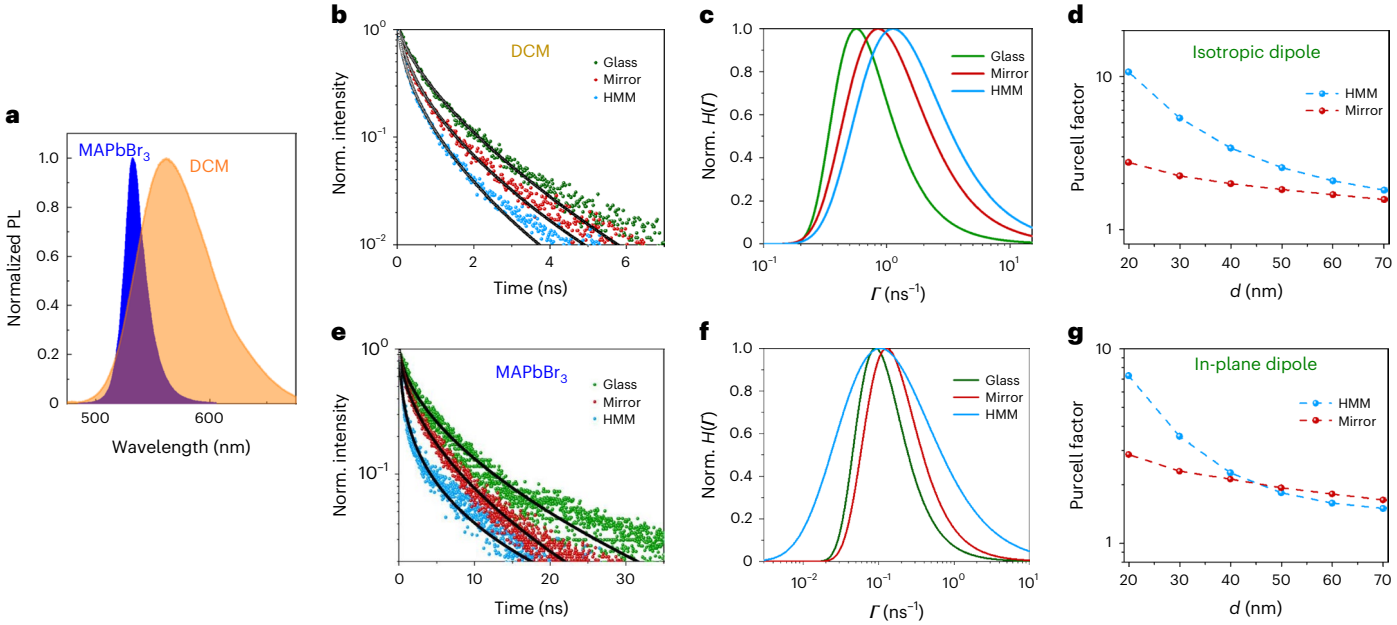

Fig. 3 | TRPL results of $MAPbBr_3$ and DCM films. a, PL spectra of $MAPbBr_3$ (blue) and DCM (yellow) films deposited on glass at 470-nm excitation. **b**,**c**, Experimental results for normalized time-resolved PL (**b**) and calculated recombination rate distribution $H(\Gamma)$ (**c**) of DCM film deposited on glass, mirror and HMM substrates. **d**, Cross-section of PF calculation as a function of d with a mirror and an HMM for isotropic dipoles at $\lambda = 540$ nm. **e**,**f**, Experimental result of normalized time-resolved PL (**e**) and calculated recombination rate distribution $H(\Gamma)$ (**f**) of $MAPbBr_3$ polycrystalline film deposited on glass, mirror and HMM substrates. **g**, Cross-section of the PF calculation as a function of d with a mirror and an HMM for in-plane dipoles at $\lambda = 540$ nm. The filled black circles in **b** and **e** are the fitting curves based on the stretched exponential function. The excitation wavelength for time-resolved PL is 470 nm.

anisotropy is believed to be due to the lamella characteristics of the polycrystalline film, which originate from the 2D nature of the precursor. This indicates that interlayer excitons are unlikely to be formed, and this could explain the in-plane nature of the LHP excitons[45,46]. As stated earlier, the in-plane dipole orientation of $MAPbI_3$ can be utilized to engineer the exciton's LDOS. We performed time-resolved photoluminescence (TRPL) measurements on the $MAPbI_3$ and LDS750 films deposited on glass, mirror and HMM substrates. A sufficiently low excitation fluence of 0.5 μJ cm^{-2} was maintained to avoid extraneous effects such as Auger recombination. The observed non-exponential decay is due to the strong dependence of the LDOS on the distance from a plasmonic mirror (or an HMM). We thus employ the stretched exponential function as a fitting tool for the experimental results to obtain a distribution of recombination rates Γ, $H(\Gamma)$ (Methods)[47], allowing us to quantitatively determine the modified Γ resulting from the dipole–substrate interaction.

Variation of recombination rate depending on the substrates

Figure 2d,e presents the normalized TRPL and $H(\Gamma)$ of LDS750 for the three substrates. The peak value of $H(\Gamma)$, denoted $\bar{\Gamma}$, corresponds to the most likely recombination rate. Unsurprisingly, the recombination rate of LDS750 increased for a mirror and further increased for an HMM. The calculated $\bar{\Gamma}$ for glass, mirror and HMM are $\bar{\Gamma}_{glass} = 1.02\ ns^{-1}$, $\bar{\Gamma}_{mirror} = 1.49\ ns^{-1}$ and $\bar{\Gamma}_{HMM} = 2.36\ ns^{-1}$, respectively. Considering $\bar{\Gamma}_{glass}$ to approximate the free-space rate, the ratios of the recombination rate of glass to those for the mirror and HMM are $\bar{\Gamma}_{mirror}/\bar{\Gamma}_{glass} = 1.46$ and $\bar{\Gamma}_{HMM}/\bar{\Gamma}_{glass} = 2.31$, respectively.

In contrast, we observe a significant decrease in the recombination rate of $MAPbI_3$ after introducing plasmonic substrates (Fig. 2f). In Fig. 2g, we obtained $\bar{\Gamma}_{glass} = 0.078\ ns^{-1}$, $\bar{\Gamma}_{mirror} = 0.039\ ns^{-1}$ and $\bar{\Gamma}_{HMM} = 0.057\ ns^{-1}$, yielding $\bar{\Gamma}_{mirror}/\bar{\Gamma}_{glass} = 0.51$ and $\bar{\Gamma}_{HMM}/\bar{\Gamma}_{glass} = 0.73$. This indicates twofold and 1.37-fold decreases in the recombination rate, respectively. A quantitative comparison between the experimentally obtained recombination rate and the calculated ratio shows excellent agreement, as shown in Supplementary Table 2. The observation of a decrease in recombination rate for an HMM disagrees with previous studies on HMMs[3,5]. If we take the in-plane dipole of luminescent excitons in LHPs into account, however, we find a strong agreement with the analysis presented earlier (Figs. 1b and 2c). As shown in Fig. 1b, an in-plane dipole emitting at ~750 nm and located within a range of d from ~20 nm to 80 nm from the mirror substrate experiences a suppression in the recombination rate. The stronger recombination rate reduction of the $MAPbI_3$ film on a mirror compared to the HMM results from the higher LDOS associated with the excitation of BPPs. Therefore, the reduction of recombination rate for an HMM indicates that the destructive interaction between the in-plane dipole and its image leads to a reduction of the net transition dipole moment, which dominates over the high LDOS of HMMs. The dipole–substrate distance dependence of the recombination rate was confirmed by depositing $MAPbI_3$ on an HMM with a 125-nm-thick Al_2O_3 spacer layer (Supplementary Fig. 8). The TRPL results for the $MAPbI_3$ film deposited on a quenching layer phenyl-C61-butyric acid methyl ester (PCBM) and a much thicker $MAPbI_3$ film (500 nm) further corroborate our results (Supplementary Figs. 9 and 10 and Supplementary Tables 2 and 3). Furthermore, we find that the PL quantum yield (PLQY) from the $MAPbI_3$ film decreases more than that from the LDS750 film in the presence of a plasmonic mirror, which underpins the remarkable decrease in the radiative decay rate due to the in-plane dipole orientation (Supplementary Note V and Supplementary Table 4).

By fitting the TRPL of $MAPbI_3$ film on a PCBM (quenching) layer with the diffusion model (Supplementary Note V), we estimated the diffusion coefficient to be $9.2 \times 10^{-3}\ cm^2\ s^{-1}$, yielding a diffusion length of 110 nm for $MAPbI_3$ film on a glass substrate, in agreement with previous reports[48]. The suppression of the recombination rate with mirror and HMM substrates increases the diffusion lengths to 158 nm and 130 nm, respectively (Supplementary Fig. 11). Note that decreasing the recombination rate via chemical passivation does not necessarily correspond to an increase in the diffusion length, as it can change the

https://doi.org/10.1038/s41566-022-01151-3

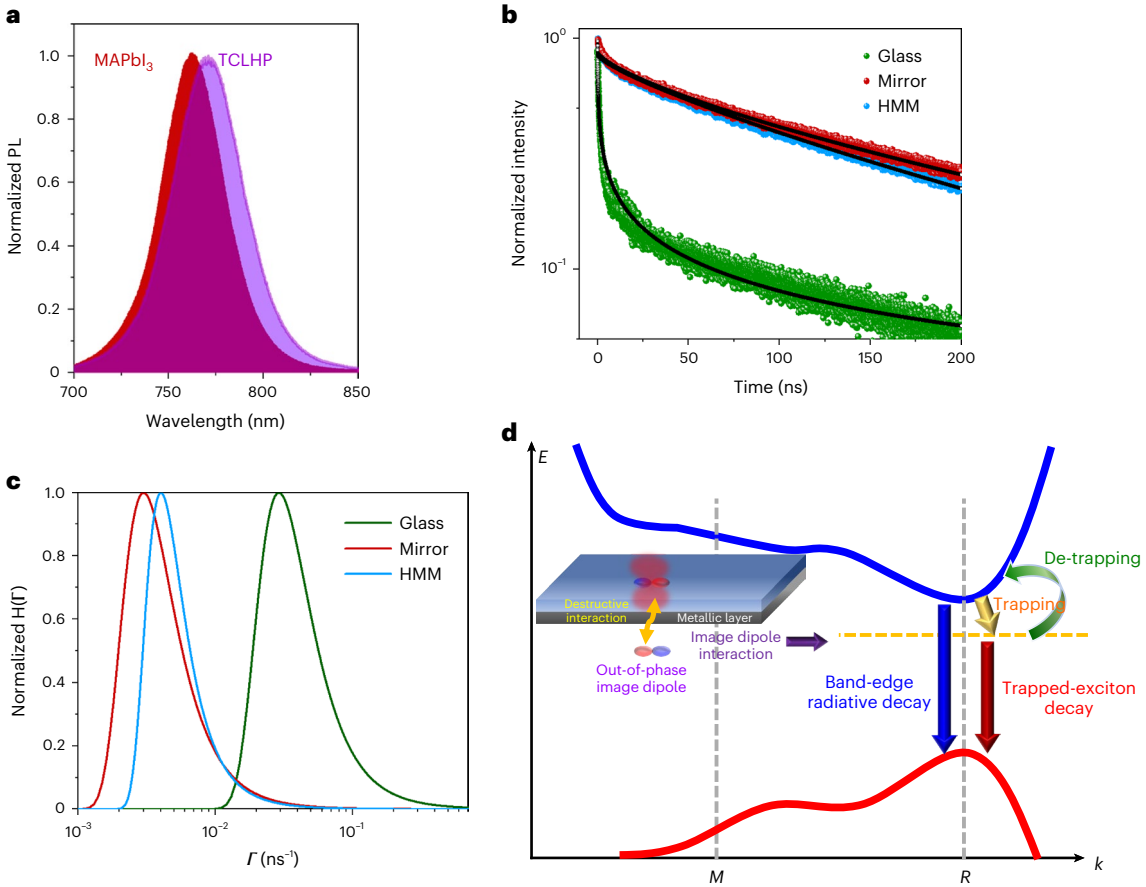

Fig. 4 | TRPL results for the TCLHP ($(Cs_{0.06}FA_{0.79}MA_{0.15})Pb(I_{0.85}Br_{0.15})_3$) film and a schematic illustration of the relevant recombination processes. a, PL spectra of $MAPbI_3$ and TCLHP polycrystalline films deposited on glass. **b**, Experimental results for normalized TRPL of TCLHP film deposited on glass, mirror and HMM substrates. **c**, Normalized recombination rate distribution $H(\Gamma)$ of TCLHP film on glass, mirror and HMM substrates. **d**, Schematics of the relevant photophysical processes in the TCLHP film by considering both image dipole interaction and trapping. The band-to-band optical transition (band-edge radiative decay) at the *R* point corresponds to the energy bandgap obtained by fitting with Elliot's formula (1.645 eV; Supplementary Table 1) for TCLHP. The yellow dashed line indicates the expected shallow trap state. Trapping and de-trapping processes as well as the direct recombination process can be affected by the image dipole interaction (Supplementary Note VII).

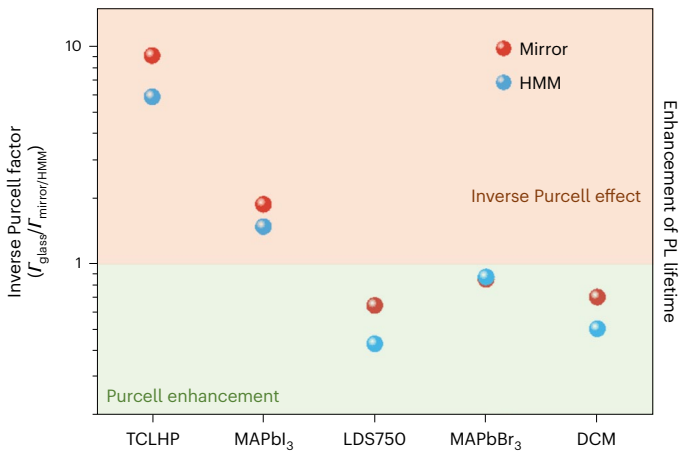

Fig. 5 | Enhancement of recombination time. Plot of the average ratio of recombination rate for glass to plasmonic-mirror and HMM substrates versus the LHPs and organic emitters used in this study. The inverse Purcell factor indicates the increase in the recombination time. The light green and light orange areas represent the decrease and increase in the recombination time.

grain boundary size in perovskites, which can adversely affect the charge mobility[16].

To examine the spectral dependence on the recombination rate, we studied another type of LHP ($MAPbBr_3$) and compared it with an organic emitter, DCM (4-dicyanomethylene-2-methyl-6-(*p*-dimethylaminostyryl)-4*H*-pyran). In Fig. 3a, both emitters exhibit a similar PL spectrum in the region where PF > 1, regardless of the dipole orientation or distance (Fig. 1b,e at $\lambda = 540$ nm). The calculated effective permittivity of the HMM shows a hyperbolic dispersion for the studied wavelength range (Supplementary Fig. 12). Figure 3b,c displays the TRPL and calculated $H(\Gamma)$ for DCM, respectively. As expected, DCM experiences a higher $\bar{\Gamma}$ for a mirror, which increases further for an HMM. A similar trend is observed for $MAPbBr_3$ (Fig. 3e), in agreement with our numerical calculations of the PF (Fig. 1b,e). The TRPL results for $MAPbBr_3$, however, exhibit a peculiar behaviour, because $H(\Gamma)$ is considerably broader for an HMM compared to that of a mirror, with faster and slower recombination rates (Fig. 3f).

Numerical calculations indicate that the broadness of $H(\Gamma)$ for $MAPbBr_3$ on an HMM substrate is due to the in-plane dipole moment of $MAPbBr_3$. Distance-dependent PFs at $\lambda = 540$ nm are shown in Fig. 3d,g for an in-plane dipole and an isotropic dipole, respectively. The observed $H(\Gamma)$ of $MAPbBr_3$ on an HMM can be attributed to the predominant in-plane dipole of $MAPbBr_3$. For an isotropic dipole, the PF of an HMM is greater than that of a mirror, irrespective of d (Fig. 3d). For an in-plane dipole, however, the recombination rate for a mirror is higher than that for an HMM when $d > 45$ nm (Fig. 3g), resulting in a broader distribution of Γ on an HMM, with faster and slower Γ components compared to that on a mirror for an in-plane dipole. The observation of lower recombination rates could be related to the strong presence of trap states in $MAPbBr_3$[49], which, as we detail later, may become

https://doi.org/10.1038/s41566-022-01151-3

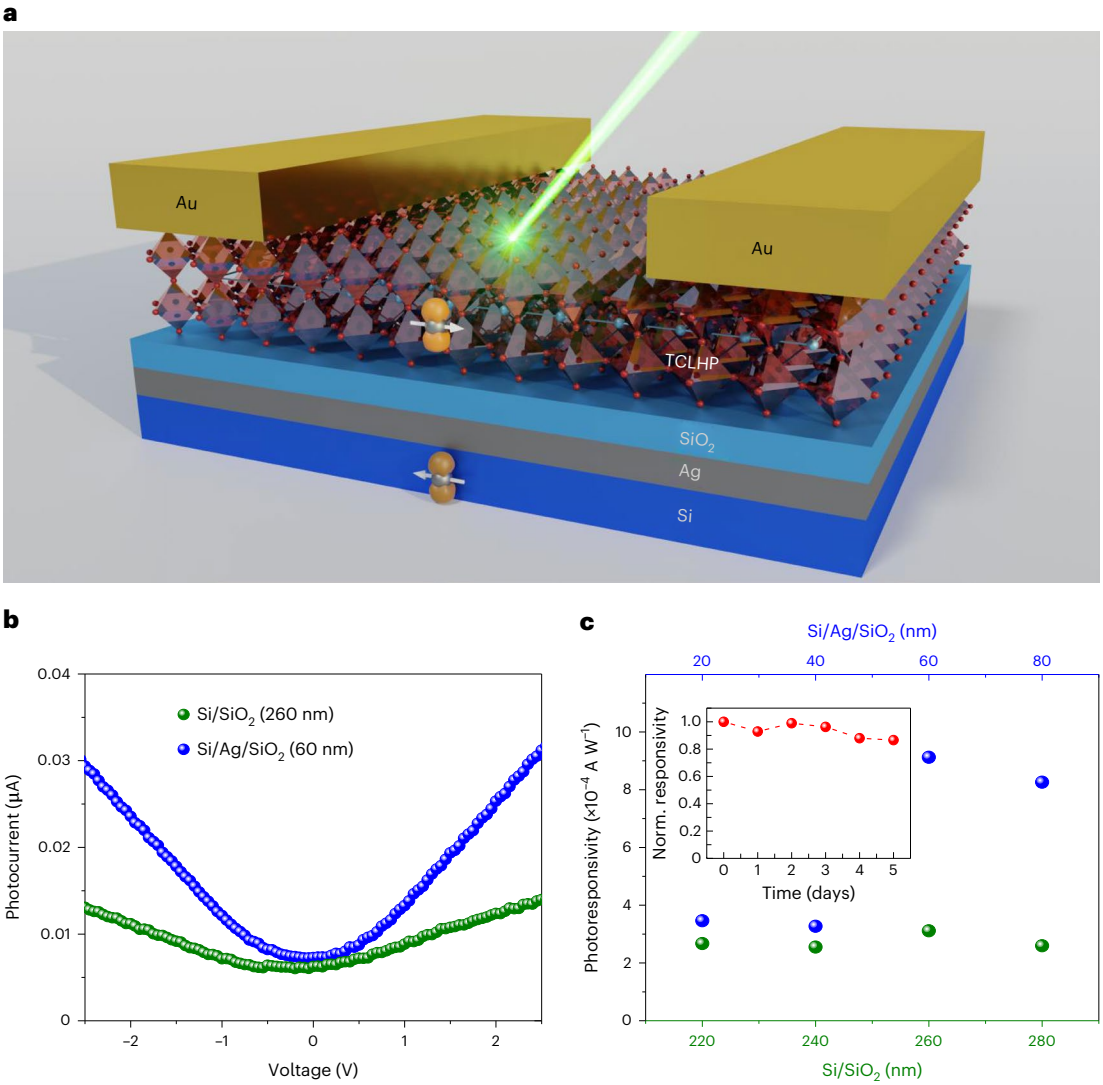

Fig. 6 | Enhanced photoresponsivity of LHPs with suppressed recombination rate. a, Photodetector structures using $(Cs_{0.06}FA_{0.79}MA_{0.15})$ $Pb(I_{0.85}Br_{0.15})_3$ as an active material, with a 50-nm-thick Ag film introduced. **b**, Measured photocurrent for the device shown in a and a reference device without an Ag mirror, as a function of voltage with 532-nm light. **c**, Photoresponsivity at $\lambda = 532$ nm with a bias voltage of −2.5 V for the device shown in **a** (blue spheres) and the reference device (green spheres). Inset: device stability of the hybrid photodetector. The responsivity remains more than 85%, even after five days.

responsible for an even slower recombination rate as they correspond to a lower transition energy compared to trap states.

To generalize our observations, we performed a TRPL study on a TCLHP ($(Cs_{0.06}FA_{0.79}MA_{0.15})$ $Pb(I_{0.85}Br_{0.15})_3$), which shows an ~20-meV redshifted PL band compared to $MAPbI_3$ (Fig. 4a), consistent with the energy-gap value extracted from the absorption spectrum (Supplementary Fig. 4b and Supplementary Table 1). TCLHPs are excellent active materials[35,50] that enjoy stronger thermal stability, less moisture susceptibility, higher fabrication tolerance and a stronger nonlinear optical response compared to $MAPbI_3$[46]. The exciton binding energy of the TCLHP (32 meV) is similar to that of $MAPbI_3$ (Supplementary Note VI). X-ray diffraction analysis of TCLHP films deposited on glass, mirror and HMM showed no significant change (Supplementary Fig. 13). Figure 4b,c presents the TRPL results and $H(\Gamma)$ of TCLHP film for different substrates. For a glass substrate, the fast decay component associated with trap-assisted recombination is pronounced, consistent with previous studies[35]. Introducing plasmonic substrates dramatically decreases the recombination rate of the TCLHP. In Fig. 4d, we describe the band-structure of TCLHP[50], as well as the relevant photophysical processes. The reduction in the PLQY indicates that the trapping process becomes slower and carriers in the trap states live longer (Supplementary Note VII), so the carriers in the trap states are likely to de-trap and decay with a longer time from the conduction band-edge, leading to the giant reduction in the recombination rate (Supplementary Fig. 14). Numerical simulations of the depopulation dynamics based on the coupled differential rate equations reflecting the longer radiative and trapping processes support this interpretation (Supplementary Fig. 18 and Supplementary Table 5). In Fig. 5 we plot $\bar{\Gamma}_{glass}/\bar{\Gamma}_{mirror}$ and $\bar{\Gamma}_{glass}/\bar{\Gamma}_{HMM}$ versus the perovskite and organic films used in this work, obtaining a value of 0.11, and for TCLHP film, obtaining 0.16. This indicates an approximately tenfold (~900%) and sixfold (500%) decrease (increase) in recombination rate (recombination time) in the presence of a mirror and HMM, respectively. This giant reduction of the recombination rate is even higher than predicted numerically and indicates the existence of another mechanism. The results of $H(\Gamma)$ show that suppression of the recombination rate occurs for all the decay-rate components, including the fast decay associated with trap states (Fig. 4c). We believe that this is related to the de-trapping of excitons from trap states back to the band-edge, which is more likely to take place at room temperature due to thermal excitations[51]. We note that this physical suppression

of trap states does not affect the mobility and morphology of perovskite, enabling effective minimization of the influence of trap states without chemical drawbacks such as reduction of mobility[16].

Enhanced photoresponsivity of hybrid photodetectors

The observed reduction in the recombination rate and the associated increase in the diffusion length open the door to enhancing the performance of LHP-based devices. Figure 6a presents a schematic of an LHP-based photodetector with a plasmonic mirror (hybrid photodetector). We fabricated a set of devices by varying the spacer layer thickness and with a TCLHP as active material. For the conventional photodetector, used as a reference, we fabricated four samples with different SiO_2 spacer layer thickness (from 220 nm to 280 nm). The proposed hybrid device introduces a 50-nm-thick silver (Ag) layer on top of the silicon substrate. The SiO_2 spacer layer between the Ag film and the active material was varied from 20 nm to 80 nm. TCLHP films were deposited onto all the substrates, followed by deposition of 80-nm Au counter electrodes via thermal evaporation. For all the devices, we measured the photocurrent and photoresponsivity (R) generated by the power of the incident light at 532 nm, expressed by the following equation:

$$R = \frac{I_{\text{light}} - I_{\text{dark}}}{P}$$

where I_{light}, I_{dark} and P are the photocurrent, dark current and incident light power density, respectively. Figure 6b shows the photocurrent as a function of voltage for both conventional and hybrid photodetectors with 260-nm- and 60-nm-thick SiO_2 layers, respectively (the data for all devices are presented in Supplementary Fig. 15). The photocurrent obtained from the hybrid photodetector is remarkably higher than that obtained from the conventional photodetector. The higher photocurrent in the presence of a metal layer leads to higher photoresponsivity R. Figure 6c shows the R at a bias voltage of −2.5 V for all devices. Although R remains nearly constant for the conventional devices when varying the SiO_2 thickness, it increases significantly for the hybrid devices in an appropriate SiO_2 thickness range. In particular, R increases by 250% in the hybrid photodetector for 60-nm SiO_2 layers compared to conventional photodetectors. We note that the change in optical absorption due to introducing the metal layer plays no crucial role in increasing the photocurrent (Supplementary Fig. 16). In addition, a decrease in LDOS in the broad range of the emission band leading to a longer carrier lifetime does not necessarily correspond to a reduction of LDOS in the absorption band (Fig. 1b). Therefore, the enhancement in R is attributed to the slower exciton recombination and longer diffusion length in perovskite resulting from the in-plane dipole–image dipole interaction. Along with the demonstrated stability of the hybrid photodetector (Fig. 6c, inset), the observed enhancements in the photocurrent and photoresponsivity demonstrate the potential of our hybrid device approach for developing high-performance perovskite-based optoelectronic devices.

Conclusion

In summary, we have demonstrated that the orientation of LHP excitons enables control over their recombination process. We show that the interaction between the in-plane dipole of LHP and its image formed on a plasmonic substrate decreases the recombination rate, without any chemical treatment, introduction of an optical cavity or photonic-bandgap engineering. Perhaps more surprising is the remarkable (up to sixfold) decrease in recombination rate even on an HMM substrate. By analysing the decay rate distribution, we demonstrate that, for TCLHPs, the decay channel due to trap states can be significantly suppressed due to the image dipole interaction, resulting in a tenfold increase in exciton lifetime. Furthermore, the image dipole interaction enables us to substantially improve the device performance of photodetectors by achieving a more than 250% increase in photoresponsivity. These results provide a fundamental understanding of the transition dipole properties in LHPs, which will pave the way towards physical control over the recombination process in LHPs, with far-reaching implications in optoelectronics.

Online content

Any methods, additional references, Nature Portfolio reporting summaries, source data, extended data, supplementary information, acknowledgements, peer review information; details of author contributions and competing interests; and statements of data and code availability are available at https://doi.org/10.1038/s41566-022-01151-3.

References

1. Pelton, M. Modified spontaneous emission in nanophotonic structures. *Nat. Photon.* **9**, 427–435 (2015).
2. Akselrod, G. M. et al. Probing the mechanisms of large Purcell enhancement in plasmonic nanoantennas. *Nat. Photon.* **8**, 835–840 (2014).
3. Lu, D., Kan, J. J., Fullerton, E. E. & Liu, Z. Enhancing spontaneous emission rates of molecules using nanopatterned multilayer hyperbolic metamaterials. *Nat. Nanotechnol.* **9**, 48–53 (2014).
4. Poddubny, A., Iorsh, I., Belov, P. & Kivshar, Y. Hyperbolic metamaterials. *Nat. Photon.* **7**, 958–967 (2013).
5. Krishnamoorthy, H. N. S., Jacob, Z., Narimanov, E., Kretzschmar, I. & Menon, V. M. Topological transitions in metamaterials. *Science* **336**, 205–209 (2012).
6. Purcell, E. M. Resonance absorption by nuclear magnetic moments in a solid. *Phys. Rev.* **69**, 37–38 (1946).
7. Drexage, K. H. Influence of a dielectric interface on fluorescence decay time. *J. Lumin.* **1–2**, 693–701 (1970).
8. Peter, Lodahl et al. Controlling the dynamics of spontaneous emission from quantum dots by photonic crystals. *Nature* **430**, 654–657 (2004).
9. Elkabbash, M. et al. Cooperative energy transfer controls the spontaneous emission rate beyond field enhancement limits. *Phys. Rev. Lett.* **122**, 203901 (2019).
10. Russell, K. J., Liu, T. L., Cui, S. & Hu, E. L. Large spontaneous emission enhancement in plasmonic nanocavities. *Nat. Photon.* **6**, 459–462 (2012).
11. Yablonovitch, E. & Gmitter, T. J. Photonic band structure: the face-centered-cubic case. *Phys. Rev. Lett.* **63**, 1950–1953 (1989).
12. Rogers, T. J., Deppe, D. G. & Streetman, B. G. Effect of an AlAs/GaAs mirror on the spontaneous emission of an InGaAs-GaAs quantum well. *Appl. Phys. Lett.* **57**, 1858–1860 (1990).
13. Haroche, S. & Kleppner, D. Cavity quantum electrodynamics. *Phys. Today* **42**, 24–30 (1989).
14. Barnes, W. L. Fluorescence near interfaces. *J. Mod. Opt.* **45**, 661–699 (1998).
15. Brotons-Gisbert, M. et al. Out-of-plane orientation of luminescent excitons in two-dimensional indium selenide. *Nat. Commun.* **10**, 3913 (2019).
16. Scott, R. et al. Directed emission of CdSe nanoplatelets originating from strongly anisotropic 2D electronic structure. *Nat. Nanotechnol.* **12**, 1155–1160 (2017).
17. Wang, G. et al. In-plane propagation of light in transition metal dichalcogenide monolayers: optical selection rules. *Phys. Rev. Lett.* **119**, 047401 (2017).
18. Schuller, J. A. et al. Orientation of luminescent excitons in layered nanomaterials. *Nat. Nanotechnol.* **8**, 271–276 (2013).
19. Wang, X. et al. Highly anisotropic and robust excitons in monolayer black phosphorus. *Nat. Nanotechnol.* **10**, 517–521 (2015).
20. DeCrescent, R. A. et al. Bright magnetic dipole radiation from two-dimensional lead-halide perovskites. *Sci. Adv.* **6**, eaay4900 (2020).

21. Chuang, S. Y., Yu, C. C., Chen, H. L., Su, W. F. & Chen, C. W. Exploiting optical anisotropy to increase the external quantum efficiency of flexible P3HT:PCBM blend solar cells at large incident angles. *Sol. Energy Mater. Sol. Cells* **95**, 2141–2150 (2011).
22. Böhmler, M. et al. Enhancing and redirecting carbon nanotube photoluminescence by an optical antenna. *Opt. Express* **18**, 16443 (2010).
23. Yang, Y. et al. Observation of a hot-phonon bottleneck in lead-iodide perovskites. *Nat. Photon.* **10**, 53–59 (2016).
24. Dong, Q. et al. Electron-hole diffusion lengths >175 μm in solution-grown $CH_3NH_3PbI_3$ single crystals. *Science* **347**, 967–970 (2015).
25. Giovanni, D. et al. Origins of the long-range exciton diffusion in perovskite nanocrystal films: photon recycling vs exciton hopping. *Light Sci. Appl.* **10**, 1–9 (2021).
26. Hu, W. et al. Germanium/perovskite heterostructure for high-performance and broadband photodetector from visible to infrared telecommunication band. *Light Sci. Appl.* **8**, 106 (2019).
27. Leung, S. F. et al. A self-powered and flexible organometallic halide perovskite photodetector with very high detectivity. *Adv. Mater.* **30**, 1704611 (2018).
28. Saidaminov, M. I. et al. Planar-integrated single-crystalline perovskite photodetectors. *Nat. Commun.* **6**, 8724 (2015).
29. Fang, Y., Dong, Q., Shao, Y., Yuan, Y. & Huang, J. Highly narrowband perovskite single-crystal photodetectors enabled by surface-charge recombination. *Nat. Photon.* **9**, 679–686 (2015).
30. Lin, Q., Armin, A., Nagiri, R. C. R., Burn, P. L. & Meredith, P. Electro-optics of perovskite solar cells. *Nat. Photon.* **9**, 106–112 (2015).
31. Jeon, N. J. et al. Compositional engineering of perovskite materials for high-performance solar cells. *Nature* **517**, 476–480 (2015).
32. Huang, J. Resolving spatial and energetic distributions of trap states in metal halide perovskite solar cells. *Science* **367**, 1352–1358 (2020).
33. Tan, Z. K. et al. Bright light-emitting diodes based on organometal halide perovskite. *Nat. Nanotechnol.* **9**, 687–692 (2014).
34. Kim, Y. H., Cho, H. & Lee, T. W. Metal halide perovskite light emitters. *Proc. Natl Acad. Sci. USA* **113**, 11694–11702 (2016).
35. Lin, K. et al. Perovskite light-emitting diodes with external quantum efficiency exceeding 20 per cent. *Nature* **562**, 245–248 (2018).
36. Chamoli, S. K., ElKabbash, M., Zhang, J. & Guo, C. Dynamic control of spontaneous emission rate using tunable hyperbolic metamaterials. *Opt. Lett.* **45**, 1671–1674 (2020).
37. Lee, K. J., Lee, Y. U., Kim, S. J. & André, P. Hyperbolic dispersion dominant regime identified through spontaneous emission variations near metamaterial interfaces. *Adv. Mater. Interfaces* **5**, 1701629 (2018).
38. Tumkur, T. et al. Control of spontaneous emission in a volume of functionalized hyperbolic metamaterial. *Appl. Phys. Lett.* **99**, 2011–2014 (2011).
39. Chen, X., Lu, H., Yang, Y. & Beard, M. C. Excitonic effects in methylammonium lead halide perovskites. *J. Phys. Chem. Lett.* **9**, 2595–2603 (2018).
40. Saba, M. et al. Correlated electron–hole plasma in organometal perovskites. *Nat. Commun.* **5**, 5049 (2014).
41. Yang, Y. et al. Large polarization-dependent exciton optical Stark effect in lead iodide perovskites. *Nat. Commun.* **7**, 12613 (2016).
42. Lee, K. J. et al. Exciton dynamics in two-dimensional MoS_2 on hyperbolic metamaterial-based nanophotonic platform. *Phys. Rev. B* **101**, 041405(R) (2020).
43. Lee, K. J. et al. Blue-shifting intramolecular charge transfer emission by nonlocal effect of hyperbolic metamaterials. *Nano Lett.* **18**, 1476–1482 (2018).
44. Lee, K. J. et al. Charge-transfer dynamics and nonlocal dielectric permittivity tuned with metamaterial structures as solvent analogues. *Nat. Mater.* **16**, 722–730 (2017).
45. Barrit, D. et al. Impact of the solvation state of lead iodide on its two-step conversion to $MAPbI_3$: an in situ investigation. *Adv. Funct. Mater.* **29**, 1807544 (2019).
46. Syed, H. et al. Giant nonlinear optical response in triple cation halide mixed perovskite films. *Adv. Opt. Mater.* **8**, 1901766 (2020).
47. Berberan-Santos, M. N., Bodunov, E. N. & Valeur, B. Mathematical functions for the analysis of luminescence decays with underlying distributions 1. Kohlrausch decay function (stretched exponential). *Chem. Phys.* **315**, 171–182 (2005).
48. Alcocer, M. J. P., Leijtens, T., Herz, L. M., Petrozza, A. & Snaith, H. J. Electron-hole diffusion lengths exceeding trihalide perovskite absorber. *Science* **342**, 341–344 (2013).
49. Shi, J. et al. Exciton character and high-performance stimulated emission of hybrid lead bromide perovskite polycrystalline film. *Adv. Opt. Mater.* **8**, 1902026 (2020).
50. Abdi-Jalebi, M. et al. Maximizing and stabilizing luminescence from halide perovskites with potassium passivation. *Nature* **555**, 497–501 (2018).
51. Goodman, A. J., Willard, A. P. & Tisdale, W. A. Exciton trapping is responsible for the long apparent lifetime in acid-treated MoS_2. *Phys. Rev. B* **96**, 121404(R) (2017).

Methods

Sample preparation

All chemicals were purchased commercially and used as received. $MAPbI_3$ precursor solutions were synthesized by mixing MAI and lead iodide (PbI_2) in a 1:1 (0.082:0.029 g) equimolar ratio in *N*,*N*-dimethylformamide (DMF; 0.7 ml) and dimethyl sulfoxide (DMSO; 0.3 ml) at 70 °C, then stirring for 6 h inside a nitrogen-filled glove box. The HMM substrates were first treated in oxygen plasma for 1 min and then transferred into the glove box. $MAPbI_3$ precursor solution (70 µl) was dropped onto the substrates, which were then spin-coated at 500 r.p.m. (for 5 s) and 2,000 r.p.m. (for 60 s). Chlorobenzene (500 µl) was dropped 20 s later. The substrates were then placed on a hotplate at 70 °C and 105 °C for 2 min and 10 min, respectively. The $MAPbBr_3$ precursor solutions were prepared by adding 0.25 mmol MABr and 0.25 mmol $PbBr_2$ in DMSO (1 ml), followed by stirring at 500 r.p.m. for 6 h in a glove box. The oxygen plasma treatment method was as described above. $MAPbBr_3$ precursor solution (70 µl) was dropped onto the substrates, then spin-coated at 500 r.p.m. (5 s) and 2,000 r.p.m. (60 s). Methylbenzene (500 µl) was dropped 35 s later.

The $(Cs_{0.06}FA_{0.79}MA_{0.15})Pb(I_{0.85}Br_{0.15})_3$ film was synthesized by following the reported two-step and anti-solvent method. With this method, we prepared a precursor solution of PbI_2 (1.2 M), FAI (1.11 M), MABr (0.21 M) and $PbBr_2$ (0.21 M) in a mixer of DMF:DMSO (4:1 volume ratio, vol/vol), followed by the addition of 5 vol% from CsI stock solution (1.5 M in DMSO), and then filtered it using a polytetrafluoroethylene membrane filter (0.2-µm pore size) to produce the final $(Cs_{0.06}FA_{0.79}MA_{0.15})Pb(I_{0.85}Br_{0.15})_3$ precursor solution. This precursor solution was spin-coated on the glass slide using a two-step process at 2,000 and 6,000 r.p.m. for 10 s and 30 s, respectively. After a set time, another solvent, chlorobenzene (190 µl), was added to the substrate for 30 s while spinning. Subsequently, the substrate was thermally annealed at 100 °C for 1 h, then preserved in a nitrogen-filled glove box.

DCM and LDS750 were blended into a poly(methyl methacrylate) host (2 wt%) to prevent the quenching effect due to aggregation, and deposited by spin-coating at 3,000 r.p.m. for 30 s.

The multi-layered HMM, consisting of four pairs of alternating 10-nm-thick Ag–Al_2O_3 layers, was fabricated by electron-beam evaporation.

Calculation of the PF

We performed a finite-difference time-domain (FDTD) simulation, using Lumerical software, to calculate the PF (*F*) and the external quantum efficiency (*f*). We also verified the calculations for *F* and *f* using an FDTD stack optical solver. The calculation procedure is as follows: an electric dipole (representing a quantum emitter) is placed 10 nm above the HMM surface, and the dipole orientation is assumed to be isotropic with respect to the interface:

$$\text{Power density}\,(F_{\text{rad}}) = \frac{P_{\text{rad}}}{P_0}$$

$$\text{Quantum efficiency}\,(f) = \frac{F_{\text{rad}}}{F}$$

where *F* is the Purcell factor (PF), P_{rad} is the power emitted in the far-field, $P_{\text{non-rad}}$ is the power dissipated non-radiatively, for example, by exciting an SPP or a BPP, and P_0 is the power emitted by the dipole in an infinite uniform medium. The quantum efficiency *f* is given by the ratio of the power density, F_{rad}, and the PF, *F*.

Absorption, PL and Raman spectra measurement

UV–vis absorption measurements were carried out on all samples using a Cary 5000 UV-visible-NIR spectrometer (Agilent). The Raman and PL signals were collected by a LabRAM HR Evolution Raman spectrometer (Horiba Jobin Yvon, ×100 objective (numerical aperture = 0.9) and 1,800-lines-per-mm gratings). The laser excitation was at 532 nm and a power of 0.1 milli-watts.

TRPL measurement

TRPL measurements were carried out using a time-correlated single photon counting system (PicoQuant) excited with a 532-nm laser with 150-ps pulse duration. The excitation fluence was maintained at 0.5 µJ cm^{-2} for each entire measurement.

Analysis of TRPL results based on the stretched exponential function

The decay dynamics of the current system is complicated as it allows for various decay processes and a spatially varying LDOS. The main advantage of the stretched exponential fitting method is that it takes into account all processes for our system. In such cases, the fluorescence decay can be written as[47]

$$I(t) = \int_0^\infty H(\Gamma)\ \exp(-\Gamma t)\mathrm{d}\Gamma \tag{M1}$$

where Γ is the decay rate and $H(\Gamma)$ is a distribution of the decay rates. Here we assume that the fluorescence decay follows a stretched exponential (Kohlrausch) function such that[47]

$$I(t) = \exp[-(t/\tau_0)^\beta] \tag{M2}$$

where $0 < \beta \leq 1$, and τ_0 is a parameter with the dimensions of time. Determination of $H(\Gamma)$ from experimental data (that is, for a given $I(t)$) can be obtained with[47]

$$H(\Gamma) = \frac{\tau_0}{\pi}\int_0^\infty \exp\left[-u^\beta \cos(\beta\pi/2)\right]\cos[u^\beta \sin(\beta\pi/2) - \Gamma\tau_0 u]\ \mathrm{d}u \tag{M3}$$

Fabrication and characterization of photodetectors

To fabricate hybrid horizontal photodetector, the perovskite $(Cs_{0.06}FA_{0.79}MA_{0.15})Pb(I_{0.85}Br_{0.15})_3$ film was spin-coated on the Si/SiO_2 or $Si/Ag/SiO_2$ substrate, then an 80-nm gold electrode was evaporated on top of the perovskite. A silver layer was deposited on the silicon substrate using electron-beam evaporation. The *I*–*V* curves were measured at room temperature in an ambient atmosphere with a Keithley 4200A semiconductor parametric analyser (Tektronix) and a C-100 probe station from TPSi Company. All the photoresponse characteristics of the devices were measured under 532-nm laser excitation with tunable light intensity.

Data availability

The data that support the findings of this study are available from the corresponding author upon reasonable request.

Acknowledgements

This research was supported by the Bill and Melinda Gates Foundation, the Army Research Office, the National Science Foundation and the National Natural Science Foundation.

Author contributions

K.J.L., M.E. and C.G. discussed and defined the project. K.J.L. and M.E. initiated the project and designed and coordinated the experiments. Y.W. characterized the optical properties of the samples. R.W. prepared the nanophotonic substrates and performed numerical calculations of absorption. K.J.L. and Y.W. performed TRPL measurements. K.J.L. and J.Z. carried out the radiation pattern measurements. S.K.C. and M.E. performed the Purcell factor calculations. W.K., T.H. and W.Y. carried out the photodetector experiment. K.J.L., M.E. and C.G. analysed the

data. K.J.L., M.E. and C.G. wrote the manuscript. C.G. supervised the overall project. All authors commented on the paper.

Competing interests
The authors declare no competing interests.

Additional information
Supplementary information The online version contains supplementary material available at https://doi.org/10.1038/s41566-022-01151-3.

Correspondence and requests for materials should be addressed to Kwang Jin Lee, Mohamed ElKabbash or Chunlei Guo.

Peer review information *Nature Photonics* thanks Takashi Asano, Matthew Pelton and the other, anonymous, reviewer(s) for their contribution to the peer review of this work.